

# Engineering of Hydrogenated (6,0) Single-Walled Carbon Nanotube under Applied Uniaxial Stress: A DFT-1/2 and Molecular Dynamics Study

Yumnam Thakur Singh, Bhanu Chettri, Lalrin Kima, Zosiamliana Renthlei, Prasanta Kumar Patra, Mattipally Prasad, Juluru Sivakumar, Amel Laref, Madhav Prasad Ghimire,\* and Dibya Prakash Rai\*



Cite This: *ACS Omega* 2023, 8, 6895–6907



Read Online

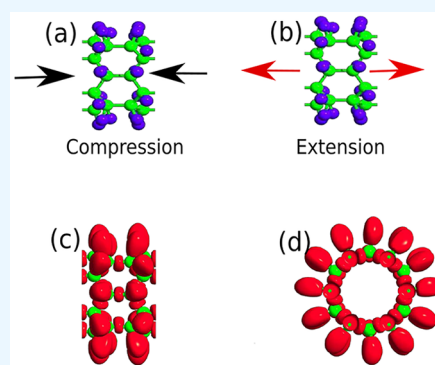
ACCESS |

Metrics & More

Article Recommendations

Supporting Information

**ABSTRACT:** Herein, we systematically studied the electronic, optical, and mechanical properties of a hydrogenated (6,0) single-walled carbon nanotube [(6,0) h-SWCNT] under applied uniaxial stress from first-principles density functional theory (DFT) and molecular dynamics (MD) simulation. We have applied the uniaxial stress range from  $-18$  to  $22$  GPa on the (6,0) h-SWCNT ( $-$  sign indicates compressive and  $+$  indicates tensile stress) along the tube axes. Our system was found to be an indirect semiconductor ( $\Gamma-\Delta$ ), with a band gap value of  $\sim 0.77$  eV within the linear combination of atomic orbitals (LCAO) method using a GGA-1/2 exchange-correlation approximation. The band gap for (6,0) h-SWCNT significantly varies with the application of stress. The indirect to direct band gap transition was observed under compressive stress ( $-14$  GPa). The strained (6,0) h-SWCNT showed a strong optical absorption in the infrared region. Application of external stress enhanced the optically active region from infrared to Vis with maximum intensity within the Vis-IR region, making it a promising candidate for optoelectronic devices. *Ab initio* molecular dynamics (AIMD) simulation has been used to study the elastic properties of the (6,0) h-SWCNT which has a strong influence under applied stress.



## INTRODUCTION

In recent decades, nanoscience and nanotechnology have been directed to the carbon nanostructures (graphene, diamond, nanotubes, and nanowires, etc.) due to their fascinating physical properties<sup>1–4</sup> as well as their potential application in nanoelectronics.<sup>5–8</sup> With the discovery of graphene,<sup>9</sup> other allotropes of carbon were also discovered and carbon nanotubes (CNTs) was one of them which was first discovered in 1991.<sup>10</sup> One dimensional (1D) single-walled carbon nanotubes (SWCNTs) have become a focal point for many researchers with the hope of constructing nanomechanical sensors, nanoelectronics and optoelectronic devices.<sup>11–15</sup> Many researchers have conducted extensive experimental and theoretical research on it.<sup>16–18</sup> Structurally, like in graphene, C–C bonds are formed by  $sp^2$  bonding in CNTs. The tube diameter of CNTs is in the range of nanometers and the tube length in the range of microns to centimeters. Depending upon the chirality and the number of tube walls that are arranged concentrically, CNTs can be classified as zigzag, armchair, chiral, single-walled (SW), and multiwalled (MW) carbon nanotubes (CNTs).<sup>19,20</sup>

So far, CNTs have been synthesized in laboratories from various experimental methods.<sup>21</sup> They are categorized into three methods depending upon the experimental conditions viz. (a) laser-ablation method<sup>22–24</sup> (b) arc-discharge,<sup>25–27</sup> and (c) thermal chemical vapor deposition method.<sup>28,29</sup> Laser-

ablation method gives high-quality and high-purity nanotubes, but the cost of production is high. The most cost-efficient method is the arc-discharge method. Normally CNTs are synthesized by the thermal chemical vapor deposition method and also best suited as it allows control of the experimental conditions.<sup>21</sup> CNTs, not only in pure form but also in contact with foreign elements, show unique functionality.<sup>30,31</sup> The ZnO/SWCNT network shows better CO detection ability in comparison with the ZnO cluster or with bare SWCNTs.<sup>32</sup> Wang et al.<sup>33</sup> from experimental approaches reported that CNT decorated with  $MoS_2$  shows excellent photosensing performance. Mechanically, carbon nanotube-polyurethane (CNT-PU) nanocomposite shows an excellent Young's modulus ( $E_y$ ) value of  $1.27$  GPa which is 10 times higher than normal PU.<sup>34</sup> Recently, Hu et al.,<sup>35</sup> using coarse-grained molecular dynamics (CGMD) simulations, investigated the friction behaviors and microscopic mechanism of carbon nanotube networks (CNNs) which provided a better under-

Received: December 1, 2022

Accepted: January 20, 2023

Published: February 7, 2023



standing of the structural deformation for CNNs and composites under tension, compression, and compaction. CNTs also have diverse medical applications such as stem cell differentiation and cell adhesion in designing organic as well as inorganic composites, cell compatibility, and scaffolding element.<sup>36–39</sup> As an open-mouthed structure, drug loading in CNTs is very simple. Certain types of CNTs can be internally filled with various chemicals and biochemicals with sizes ranging from small molecules to large proteins. Having the capability to carry multiple therapeutic moieties or other functional molecules, CNTs helps in probing, imaging, and targeting at specific sites.<sup>40–42</sup>

SWCNTs exhibit unconventional electronic properties; i.e., it shows different electronic behavior depending on the chirality. Several studies have reported modified electronic, optical, and mechanical behavior of SWCNT depending on their chirality,<sup>43,44</sup> doping manifestation,<sup>45–47</sup> and applied stress.<sup>48–50</sup> For nanomaterials, modification of physical behavior by doping is a standard technique as it can easily manipulate the band structure of the material by creating additional energy levels within the band gap. However, hydrogenation, which is a dopant-free and also easily controllable method, can also modify the energy band structure of nanomaterials. Hydrogenated graphene is a direct band gap insulator which is due to the formation of an *sp* bond in which the free  $\pi$ -electron of C atom couple with the 1s electron of H atom.<sup>51</sup> Guzman et al.<sup>52</sup> by using density functional theory (DFT) have investigated the band structure for a hydrogenated silicene sheet and reported the opening of the band gap to 2.2 eV. CNTs can interact with hydrogen through both physisorption and chemisorption mechanism. The possibility of hydrogen chemisorption was first reported by Yuchen et al.<sup>53</sup> through an MD simulation method which was later experimentally supported by Nikitin et al.<sup>54</sup> For hydrogen as an energy source, researchers are mostly focused on physisorption as chemisorption requires a high temperature value (approximately 1000 K) to release the hydrogen atoms from the CNT surface.<sup>54–56</sup> But Mercuri,<sup>57</sup> from the first principle MD simulation study, reported the possibility of releasing the hydrogen chemisorbed on the side wall of the (10,0) SWCNT by thermal activation at 650 K. Beyond hydrogen storage, hydrogenation can also tailor both the physical and chemical properties of nanotubes. Denis et al.,<sup>58</sup> from DFT, reported the increase in band gap for zigzag SWCNTs with an increase in hydrogen coverage. The authors also reported a band value of 3.38 eV for (16,0) SWCNT at 50% hydrogen coverage. Zhu et al.,<sup>59</sup> from the experimental approach, reported the dramatic enhancement on the field emission properties for hydrogenated TiO<sub>2</sub> nanotubes (TNAs) in comparison with pristine TNAs. Owing to high flexibility, low density, and a large aspect ratio, CNTs are also one of the most promising materials in the field of flexible strain sensors.<sup>60</sup> Yamada et al.<sup>61</sup> fabricated a wearable strain sensor containing aligned SWCNTs which have a strain measurable capacity 50 times more than conventional metal strain gauges. Zhou et al.<sup>62</sup> also designed a crack-based strain sensor with a superwide workable strain range and an ultrahigh sensitivity by spray-coating CNT ink onto an electrospun thermoplastic polyurethane fibrous mat. Recently, Choi et al.<sup>63</sup> successfully developed an asterisk-shaped carbon nanotube strain sensor having a good sensing ability at microdeformation and also able to recognize the direction of the applied tensile stress. In this study, we consider a fully hydrogenated (6,0) SWCNT

[(6,0)h-SWCNT]. After that, we have systematically investigated the electronic, optical, and mechanical properties under different strength of uniaxial compressive and tensile stress. The first principle based DFT-1/2 approach is used for electronic and optical properties calculations. For mechanical properties analysis, *ab initio* molecular dynamics (AIMD) based on DFT was employed as implemented in VNL-ATK software package<sup>64</sup>

## COMPUTATIONAL DETAILS

All of the electronic and optical properties were calculated by adopting the linear combination of atomic orbitals method (LCAO) employed in QuantumATK Q-2019.12.<sup>64</sup> To correct the self-interaction error of electrons, generalized DFT-1/2 (GGA-1/2) with Perdure–Burke–Ernzerhof formalism<sup>65,66</sup> was used as exchange–correlation functional. The complex nucleon–nucleon interaction was described based on a Pseudo-Dojo pseudopotential.<sup>67</sup> The plane wave cutoff energy was set to 55 Ha (1500 eV). In all of the electronic calculations, the first Brillouin zone integration was performed by sampling  $1 \times 1 \times 3$  k-mesh. For optical calculations, a high k-mesh value of  $1 \times 1 \times 22$  was used. We have employed the Force field method for geometry optimization using potential set “TeroffCH2005”.<sup>68</sup> No constraints were imposed in any axis during optimization.

We have checked the thermodynamic stability by calculating the phonon dispersion relation as implemented in QuantumATK Q-2019.12. To test the thermal stability, we performed *Ab Initio* Molecular Dynamics (AIMD) at room temperature (300 K) for each system. Here we opt the canonical ensemble (NVT) with constant temperature and the total time steps for each MD simulation is taken as 30 Ps. Further, we examined the structural stability by calculating the formation energies which is given by eq 1<sup>69</sup>

$$E_{\text{form}} = E_t - n_c \times E_C - n_H \times E_H \quad (1)$$

where  $E_t$  is the total energy of the (6,0) h-SWCNT,  $n_c$ ,  $n_H$ ,  $E_C$ , and  $E_H$  are the number of carbon atoms in the system, the number of hydrogen (H) atoms in the system, the chemical potential of carbon, and the chemical potential of hydrogen, respectively.

For mechanical properties, a series of MD simulations are performed for each system using the TeroffCH2005 classical potential as the potential function for two C–H atoms. Setting the reservoir temperature at 300 K, the initial velocity of the atoms are taken from the Maxwell–Boltzmann distribution. The total time steps is set at 100000 fs, and for each 1000 time steps a strain value of 0.007 is applied. The correspond stress value is calculated from eq 2<sup>70,71</sup>

$$\sigma^{\alpha\beta} = 1/V \left[ -\sum_i m_i v_i^\alpha v_i^\beta + 1/2 \sum_i \sum_{j \neq i} F_{ij}^\alpha r_{ij}^\beta \right] \quad (2)$$

where  $m_i$  and  $v_i$  are the mass and velocity of the of the  $i$ th atom,  $F_{ij}$  is the force between the  $i$ th and  $j$ th atoms,  $\alpha$  and  $\beta$  are the Cartesian components,  $V$  is the total volume occupied by all the atoms, and  $r_{ij}^\beta$  is the projection of the interatomic distance along the  $\alpha$  coordinate.

## RESULTS AND DISCUSSION

The optimized structure of the hydrogenated (6,0) SWCNT ((6,0) h-SWCNT) is shown in Figure 1. One hydrogen (H)

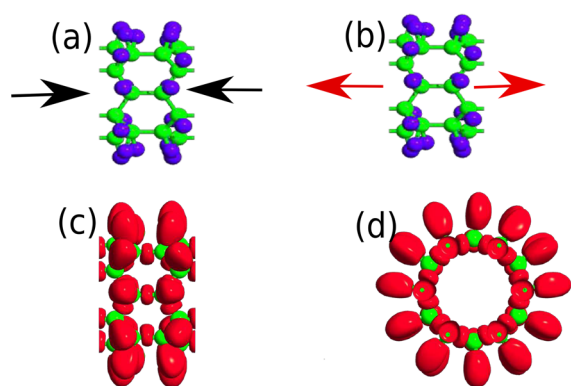


**Figure 1.** Optimized structure for (6,0)h-SWCNT with (a) compressive and (b) tensile stress. (c) Side view and (d) front view of electron localization function for (6,0)h-SWCNT.

atom is bonded with each carbon (C) atom with the bond length ( $d_{C-H}$ ) 1.32 Å. The carbon–carbon bond length ( $d_{C-C}$ ) value is 1.47 Å which is very closed to 1.52 Å.<sup>72</sup> The measured bond angles  $\theta_{C-C-H}$  and  $\theta_{C-C-C}$  are 99.27° and 188.57°, respectively. For our investigations, compressive stress (– sign) and tensile stress (+ sign) are progressively applied along the  $z$ -axis. Each structure was optimized at different applied stress. For dynamic stability analysis, we have calculated the phonon dispersion relations along the high-symmetry directions of the first Brillouin zone, and the results are shown in Figures 2 and 3). For dynamic stability calculation, we are more focused on the lower energy branches, i.e., three acoustic branches viz. the transverse acoustic branch (TA), twisting acoustic branch (TW), and longitudinal acoustic branch.<sup>73</sup> Under compressive stress, (6,0) h-SWCNT shows no negative energy up to the stress value of –3 GPa and hence

confirmed dynamical stability (figure not shown here). From stress values of –4 to –18 GPa, we have noticed small negative energies of the range  $-1 \pm 0.5$  eV. Within these stress values, TA branch and TW branch become negative showing the possibility of C–C bond bending in the nanotubes but the LA branch remains unaffected. On increasing the compressive stress beyond –18 GPa large negative energy values are observed indicating structural instability. Under tensile stress, no negative energy appeared up to the stress value of ~22 GPa, and hence, we report its dynamical stability up to ~22 GPa.

We have also analyzed the thermal stability and the structural stability for each system as well. For thermal stability analysis, each system is heat-treated at 300 K using AIMD within 30 Ps with 20000 steps. Figures 4 and 5 show the temperature fluctuation as a function of time. Throughout the MD simulation process, the temperature remains fluctuated around 300 K which shows that there is no structural transition and bond breaking in our systems up to 30 Ps of heating. Also no remarkable changes are observed in the atomic structures of the nanostructures, as presented in Figures 4 and 5. Hence, our systems are thermally stable at room temperature. To check the structural stability, we have calculated the formation energies for all the systems, and results are shown in Figure 6. The negative value in formation energy shows that (6,0)h-SWCNT is structurally stable under our reference stress values (–1 GPa to –18 GPa for compressive and 0 GPa to 22 GPa for tensile). The minimum formation energy is observed at 0 GPa, and hence, it is considered to be structurally most stable.

**Electronic Properties.** This section discusses the electronic properties of the pristine and the hydrogenated (6,0)SWCNT. DFT-1/2 method has been implemented for predicting the electronic and optical properties. From the literature,<sup>74</sup> the Heyd–Scuseria–Ernzerhof (HSE) functional

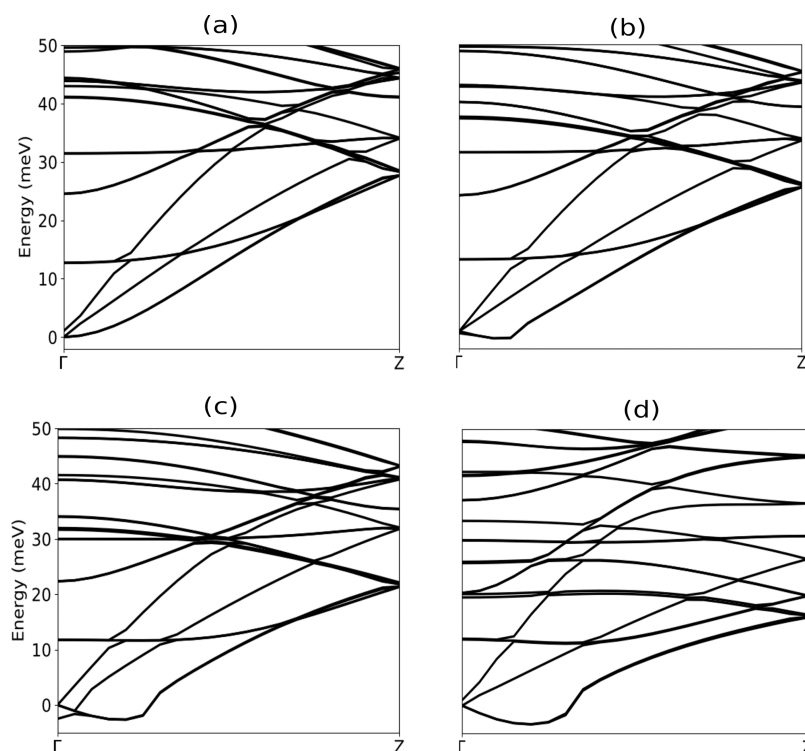


**Figure 2.** Phonon dispersion relation for (6,0) h-SWCNT with compressive stress values of (a) 0 GPa, (b) –5 GPa, (c) –10 GPa, and (d) –15 GPa.

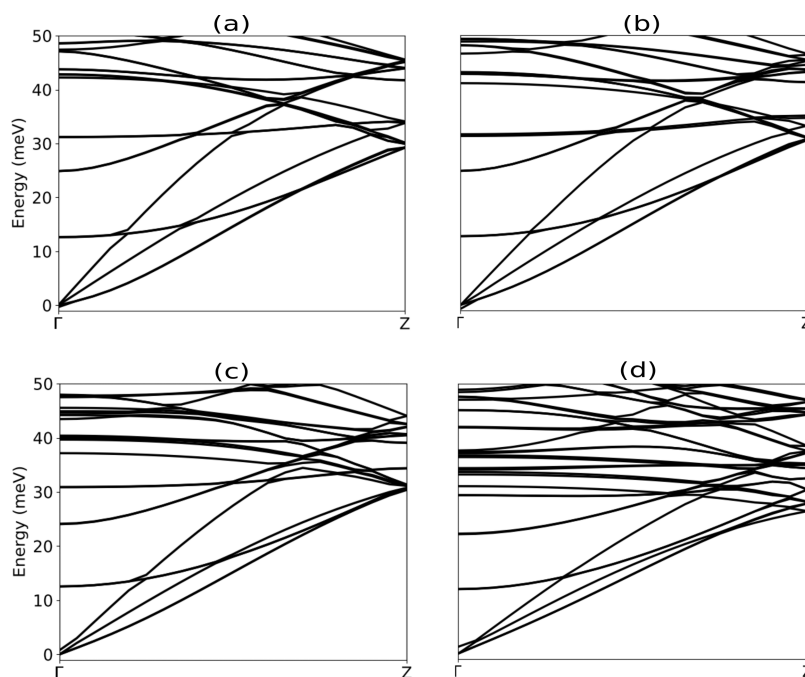


**Figure 3.** Phonon dispersion relation for (6,0)h-SWCNT with tensile stress values of (a) 5 GPa, (b) 10 GPa, (c) 15 GPa, and (d) 20 GPa.

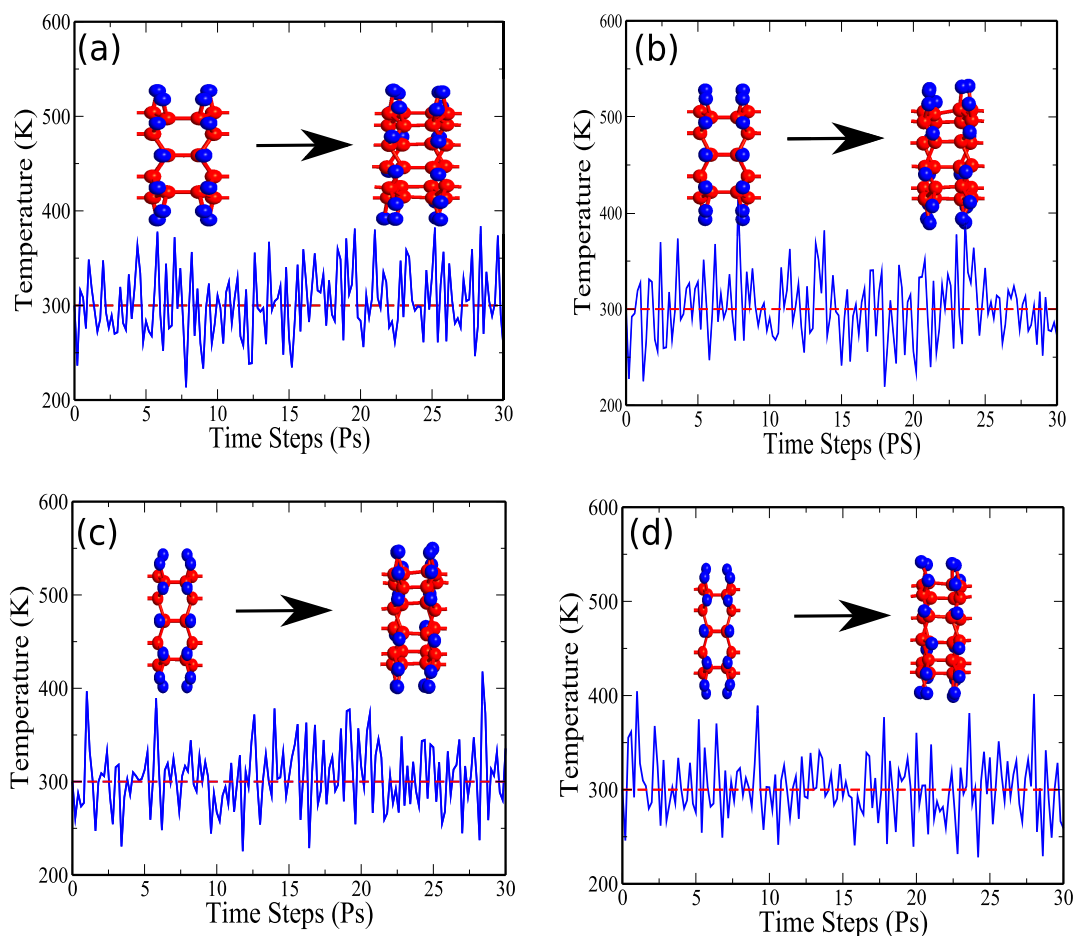


**Figure 4.** Temperature–time steps plot for (6,0)h-SWCNT with compressive values of (a) 0 GPa, (b) -5 GPa, (c) -10 GPa, and (d) -15 GPa.

also known as HSE06 is efficient in predicting the electronic and optical properties of semiconducting materials but it comes with expensive computational time and resources. On

the other hand, the DFT-1/2 approach is semilocal, and hence, the calculations converge in a more feasible time with accuracy comparable to HSE06. This method has been successfully

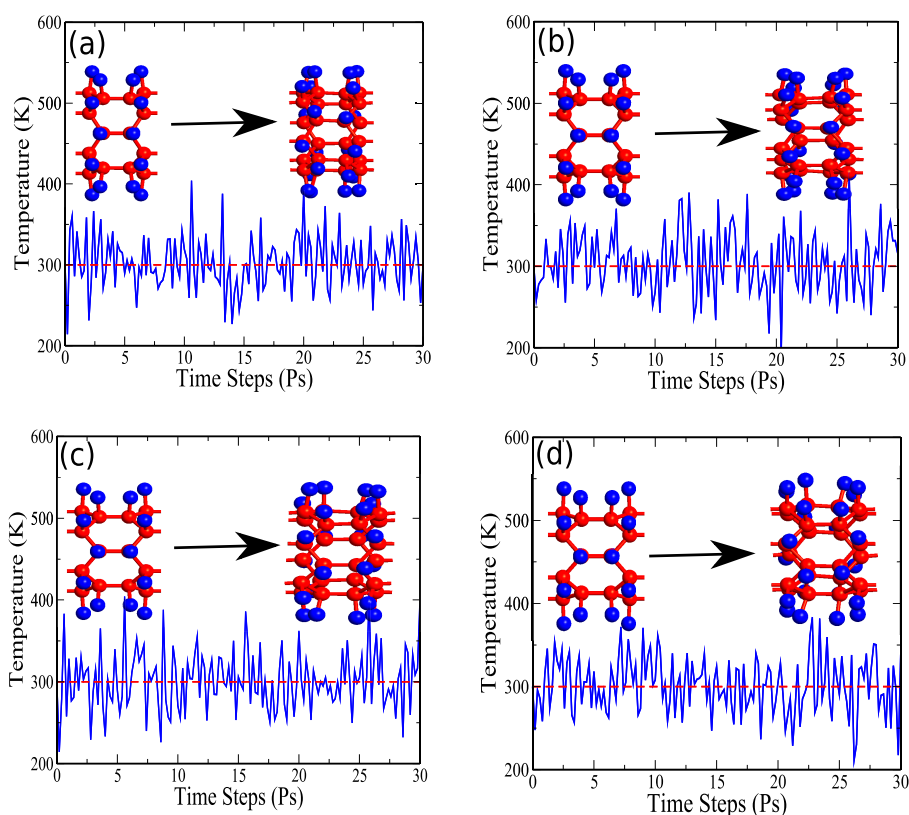


**Figure 5.** Temperature–time steps plot for (6,0)h-SWCNT with tensile stress values of (a) 5 GPa, (b) 10 GPa, (c) 15 GPa, and (d) 20 GPa.

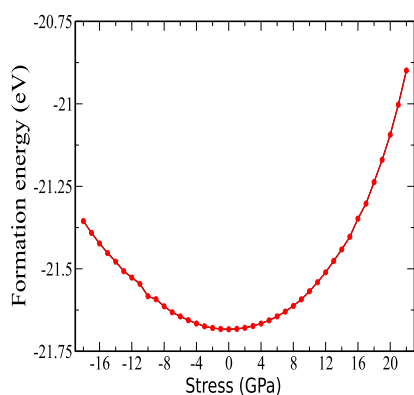


**Figure 6.** Formation energy versus stress curve for (6,0)h-SWCNT.

implemented by other researchers for predicting the electronic and optical properties of the low dimensional and bulk materials.<sup>75–77</sup> The results from HSE06 and DFT-1/2 are also presented in order to support the accuracy of the DFT-1/2 method implemented for all the calculations. The band structure plot using HSE06 is presented in Figure S1. In comparison with the DFT-1/2 approach, we have found that the band gaps resulting from HSE06 are of the same order as that of the DFT-1/2. Pristine (6,0)SWCNT is metallic in nature.<sup>78</sup> Hydrogenation results in the opening of the semiconducting band gap ( $E_g$ ) value up to 0.744 eV. The reason for such an opening in the band gap is attributed to  $sp^3$  rehybridization of the  $\pi$ -electron of C atoms with the 1s-electron of H atoms. Slijivancanin, from the DFT study of the hydrogenated (5,5) SWCNT, also reported a similar result.<sup>79</sup> The result of the partial density of states (PDOS) shows that the conduction bands are mostly contributed by H-1s states

but the valence band is primarily occupied by admixture of H-1s and C-2p states (see Figure 7a).

Figures 7 and 8 show the stress effect on the band structure and band gap. Under uniaxial compressive stress, the band gap oscillates with stress varying from  $-1$  to  $-7$  GPa. Interestingly, when the stress varies from  $-7$  to  $-18$  GPa, the band gap drops significantly which shows that (6,0)h-SWCNT is in the buckled state. As the buckling occurs, the bond lengths and bond angles of the neighboring C atoms become spatially inhomogeneous causing an abrupt change in the electronic band structure.<sup>80</sup> The maximum band gap value is observed at the stress value of  $-7$  GPa. Careful investigation of the band structures also shows that the increase of the compressive stress slowly shifts the indirect band gap for (6,0) h-SWCNT toward the direct band gap. The first indirect to direct band gap transition is observed at the stress value of  $-14$  GPa (see Table S1). Zhang et al.,<sup>81</sup> from the theoretical investigation of the phosphorene nanotube, also reported similar results. In the case of tensile stress, the band gap for (6,0) h-SWCNT evolves in two phases. The first phase corresponds to the stress value from 1 to 9 GPa and second phase from 10 to 22 GPa. In the first phase, the band gap drop significantly with an increase in stress and reaches a minimum energy value of 0.506 eV. In the second phase, the band gap increases with stress up to the maximum value of 1.001 eV. Unlike compressive stress, indirect to direct transition of the band gap is not observed in the case of tensile stress (see Table S2). More details of our calculations are shown in Tables 1 and 2.

At constant temperature, the electrical conductivity ( $\sigma$ ) of a material is inter-related with its band gap ( $E_g$ ) and can be expressed as

$$\sigma = C(\mu_e + \mu_h)eT^{3/2}e^{-E_g/2kT} \quad (3)$$

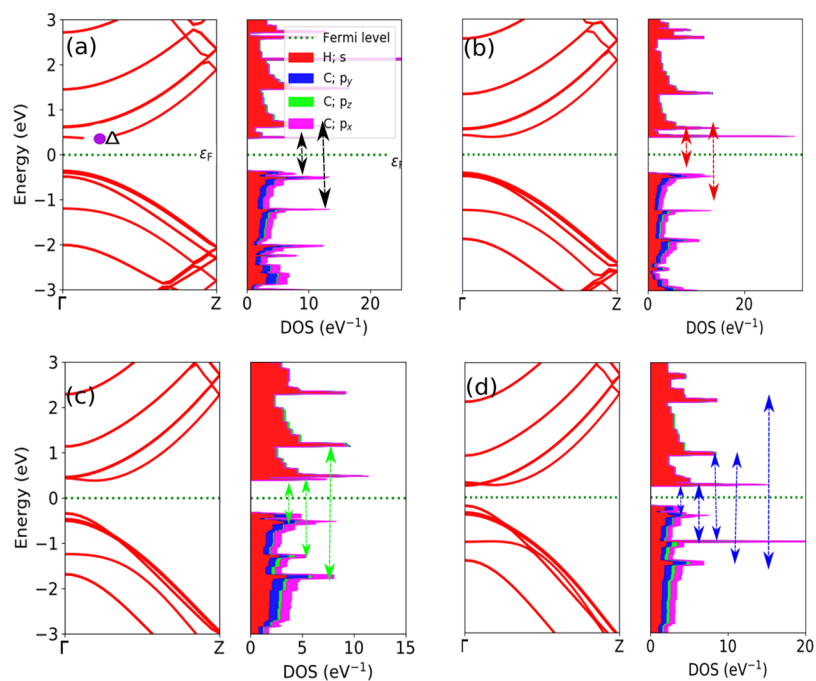


**Figure 7.** Band structure and PDOS with compressive stress (a) 0 GPa ( $\Gamma - \Delta$  transition), (b) -5 GPa, (c) -10 GPa, and (d) -15 GPa.

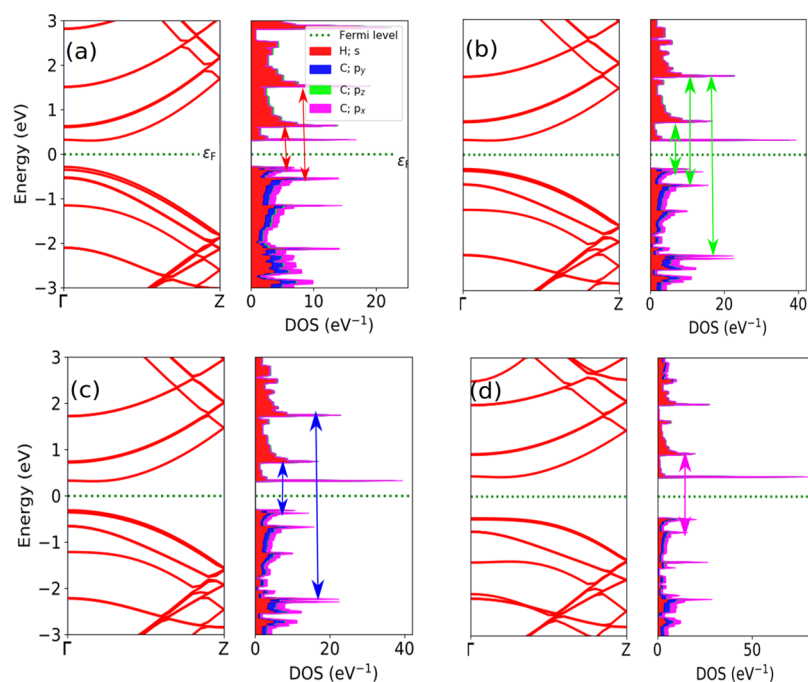


**Figure 8.** Band structure and PDOS with tensile stress (a) 5 GPa, (b) 10 GPa, (c) 15 GPa, and (d) 20 GPa.

**Table 1.** Calculated Electronic Properties for (6,0)h-SWCNT under Compressive Stress

stress (GPa)	HOMO (eV)	LUMO (eV)	direct band gap (eV)	indirect band gap (eV)
0	-0.383	0.361	0.774	0.744
-5	-0.401	0.386	0.830	0.787
-10	-0.338	0.379	0.773	0.717
-15	-0.183	0.256	0.439	0.439

**Table 2.** Calculated Electronic Properties for (6,0)h-SWCNT under Tensile Stress

stress (GPa)	HOMO (eV)	LUMO (eV)	direct band gap (eV)	indirect band gap (eV)
5	-0.289	0.301	0.609	0.590
10	-0.251	0.256	0.521	0.507
15	-0.317	0.310	0.640	0.628
20	-0.471	0.414	0.891	0.885

where  $C$  = proportionality constant;  $T$  = temperature (Kelvin);  $\mu_e$  = electron mobility;  $\mu_h$  = hole mobility;  $e$  = electron charge,

and  $k$  = Boltzmann's constant. The exponential relation between  $\sigma$  and  $E_g$  in eq 3 indicates the dramatic increase in

conductivity with small decrease in band gap. Under compressive stress, the band gap for (6,0)h-SWCNT is reduced by 70.83% (see table S1). Similarly, under extension stress, the band gap for (6,0) h-SWCNT has been reduced by 32% (see Table S2). Thus, the rough estimation indicates the possibility of enhancing the electronic conductivity for (6,0) h-SWCNT with stress application (under both compressive and tensile). For a piezo-resistive base stress sensor, the change in conductivity when stress is applied is the basic mechanism.<sup>82,83</sup> A change in conductivity with stress shows that (6,0)h-SWCNT has good potential application for a piezo-resistive base stress sensor.

To examine the ability of the (6,0) SWCNT as a host for incoming H atoms, the average adsorption energy is calculated using eq 4

$$E_{\text{ads}}(\text{eV/H}) = \frac{E_{\text{SWCNT}} + n_{\text{H}} \times E_{\text{H}} - E_{(6,0)\text{h-SWCNT}}}{n} \quad (4)$$

where  $E_{\text{SWCNT}}$ ,  $E_{\text{H}}$ ,  $E_{(6,0)\text{h-SWCNT}}$  are, respectively, the total energy for pristine (6,0) SWCNT, isolated H atom, and hydrogenated (6,0) SWCNT, and  $n$  denotes the number of hydrogen atoms.<sup>84</sup> Nikitin et al.<sup>54</sup> from the experimental approach reported the release of hydrogen from hydrogenated SWCNTs at a temperature value of 600 °C. The authors also reported the possibilities of reducing the temperature to 50–100 °C using an appropriate metal catalyst. Here, we are also reporting the reversibility kinematics (H adsorption  $\rightleftharpoons$  desorption) for all our systems by computing the desorption temperature ( $T_{\text{D}}$ ) of H atoms using Van't Hoff equation given as<sup>85</sup>

$$T_{\text{D}}(\text{K}) = \frac{|E_{\text{ads}}|}{K_{\text{B}}} \left( \frac{\Delta S}{R} - \ln P \right)^{-1} \quad (5)$$

where  $E_{\text{ads}}$  is the average adsorption energy,  $R$  is the gas constant ( $8.3145 \text{ J K}^{-1} \text{ mol}^{-1}$ ),  $K_{\text{B}}$  is the Boltzmann constant ( $1.38 \times 10^{-23} \text{ J K}^{-1}$ ),  $\Delta S$  is the change in entropy of hydrogen from gas to liquid phase, and  $P$  represents the equilibrium pressure taken as 1 atm. (6,0)h-SWCNT with no stress shows an  $E_{\text{ads}}$  value of  $-1.937 \text{ eV/H}$  and high  $T_{\text{D}}$  value of 1530.194 K. With compressive stress,  $E_{\text{ads}}$  and  $T_{\text{D}}$  values obtained are in the range of  $-1.650 \pm 0.50 \text{ eV/H}$  and  $1250 \pm 150 \text{ K}$  (see Table S3). Under extension uniaxial stress,  $E_{\text{ads}}$  and  $T_{\text{D}}$  values significantly reduce with an increase in the applied stress. At a stress value of 22 GPa, we obtain the  $T_{\text{D}}$  of 488.821 K which is near ambient temperature.<sup>86</sup> Our results show the possibility of (6,0)h-SWCNT to recognize as a safe reservoir for hydrogen storage. Table 3 shows more details of our results.

**Optical Properties.** In this section, we are investigating the stress effect on optical properties of (6,0)h-SWCNT. Here we are mostly focused on the absorption coefficient ( $\alpha_a$ ) and refractive index ( $n$ ) calculated from the dielectric function

**Table 3. Calculated Adsorption ( $E_{\text{ads}}$ ) Energies and Desorption Temperature ( $T_{\text{D}}$ ) for (6,0) h-SWCNT under Compressive and Tensile Stress (in GPa)**

Compressive	$E_{\text{ads}}$ (eV/H)	$T_{\text{D}}$ (K)	Tensile	$E_{\text{ads}}$ (eV/H)	$T_{\text{D}}$ (K)
0	-1.937	1530.194	5	-1.839	1452.843
-5	-1.960	1548.403	10	-1.670	1319.487
-10	-1.856	1457.971	15	-1.432	1131.477
-15	-1.645	1299.875	20	-0.966	762.966

$\epsilon(\omega) = \epsilon_1(\omega) + i\epsilon_2(\omega)$ . The real part  $\epsilon_1(\omega)$  characterizes the degree of polarization under an external electric field, and the imaginary part  $\epsilon_2(\omega)$  characterizes the interband electronic transition from occupied states to unoccupied states.<sup>87,88</sup>  $\epsilon_2(\omega)$  can be directly calculated from the one-electron orbitals and energies obtained from the Kohn–Sham equations. It is given by the equation below<sup>89,90</sup>

$$\epsilon_2(\omega) = \frac{\hbar^2 e^2}{\pi m^2 \omega^2} \sum_{mn'} \int_k d^3k_l \langle \vec{k}_n | \vec{p} | \vec{k}_{n'} \rangle |l^2 [1 - f(\vec{k}_n)] \delta(E_{k_n}^- - E_{k_{n'}}^- - \hbar\omega) \quad (6)$$

where  $\vec{p}$  is the momentum operator,  $|\vec{k}_n\rangle$  is the eigenfunction of the eigenvalue, and  $f(\vec{k}_n)$  is the Fermi Distribution function. The real part of the dielectric function is obtained by the Kramers–Kronig transformation from its corresponding imaginary part as

$$\epsilon_1(\omega) = 1 + \frac{2}{\pi} \int_0^\infty \frac{\epsilon_2(\omega') \omega' d\omega'}{\omega'^2 - \omega^2} \quad (7)$$

Once the  $\epsilon_1(\omega)$  and  $\epsilon_2(\omega)$  are obtained, the absorption coefficients  $\alpha(\omega)$  and refractive index  $n(\omega)$  can be calculated as

$$\alpha_a = \frac{\sqrt{2\omega(|\epsilon(\omega)| - \epsilon_1(\omega))}}{c} \quad (8)$$

where  $|\epsilon(\omega)| = \sqrt{\epsilon_1^2(\omega) + \epsilon_2^2(\omega)}$ .

$$n(\omega) = \sqrt{\frac{(\epsilon_1^2 + \epsilon_2^2)^{1/2} + \epsilon_1}{2}} \quad (9)$$

Figures 9 and 10 show our calculated  $n(\omega)$  and  $\alpha_a(\omega)$  at various stress values considering light polarized along the tube axis. For a clear illustration of our results, we are showing the plots for certain stress values. With no stress (0 GPa), the  $n$  plot for (6,0) h-SWCNT shows two prominent peaks, where the first peak is at around 1.11 eV and the second peak is at around 2.0 eV with the refractive index values of 1.14 and 1.05, respectively, and as the photon energy is further increased the  $n$  almost remains unity (see the black dotted line in Figure 9a). The calculated refractive index at the static limit ( $E = 0.0 \text{ eV}$ ) is 1.12. Similarly, as in the case of 0 GPa, the  $n$  plot for the (6,0)h-SWCNT under uniaxial compressive stress also shows two prominent peaks for each stress value (see Figure 9a). With the increase of the stress, the peak values are shifted more toward the lower energy region. However, for uniaxial tensile stress,  $n$  plot shows only one prominent peak for each different stress (see Figure 9b). In this case, the peak value shifted more toward the lower energy region with the increase of the stress, until it reached 9 GPa. From the stress value of 10 GPa, the major peaks are then shifted back to the higher energy region. In the case of both compressive and tensile stress, the higher stress value results in a higher static refractive index value and also with an increase of stress the maximum and minimum  $n$  values become higher and lower. Our results indicate that the effect of the photon energy on the refractive index of (6,0)h-SWCNT is more distinctive with the application of stress.

(6,0) h-SWCNT also shows strong optical absorption along the tube axis under uniaxial stress. With stress 0 GPa, the absorption plot for (6,0) h-SWCNT shows two distinct peaks

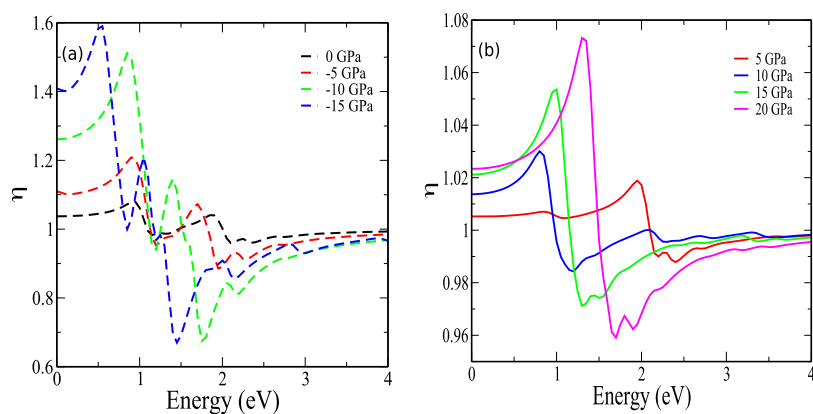


**Figure 9.** Refractive index for (6,0)h-SWCNT under (a) compressive and (b) tensile stress.

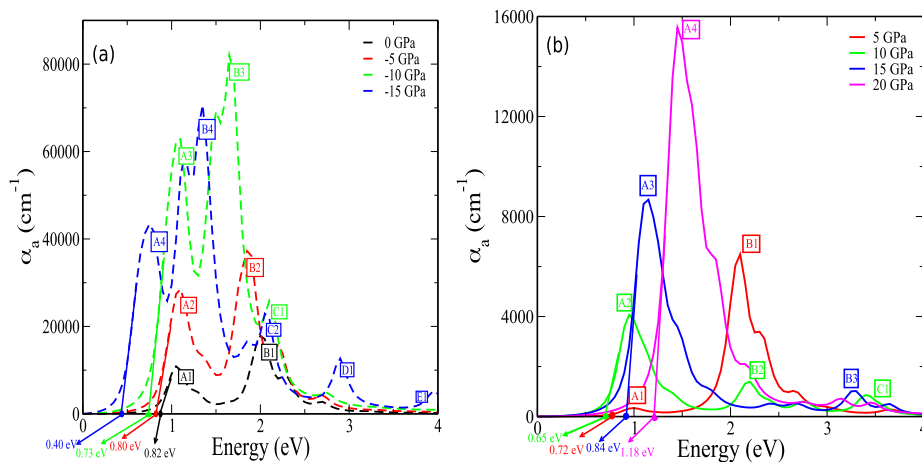


**Figure 10.** Absorption coefficient for (6,0)h-SWCNT under (a) compressive and (b) tensile stress.

(black dotted line in Figure 10a), with the lesser intensity one at 1.2 eV denoted by A1 (black) and the higher intensity one at 2.3 eV denoted by B1 (black). The optical band gap is determined by plotting a tangent along the absorption curve as shown in Figure 10. Our calculated optical band gap value for (6,0)h-SWCNT at 0 GPa is 0.82 eV which is good in agreement with the electronic band gap value. Following the band structure, PDOS (Figures 7 and 8), and absorption spectra (Figure 10), this optical band gap corresponds to the  $s$ - $p$  transition between the top of the valence and bottom of the conduction band at the  $\Gamma$ -symmetry point. The A1 (black) peak corresponds to the electronic transition between the third of the valence band to the first of the conduction band. The B1 (black) peak has the possibility transition from the fourth band of the valence band to the second of the conduction band. Under compressive stress, more distinctive absorption peaks appeared with the increase of stress and also the maximum intensity peak as well as the optical band gap shifted more toward the lower energy region (see Figure 10a). For tensile stress, the optical absorption properties evolve in two phases, the same as the electronic band structure. In the first phase (1–9 GPa), the maximum intensity peak as well as the optical band gap shifted toward the lower energy region which is contrary in the second phase (10–22 GPa). On increasing the tensile stress, we have noticed a higher number of distinctive peaks in the Vis-IR region (see Figure 10b). A strain study of zigzag  $\alpha$ -Te nanotubes by Yang et al.<sup>91</sup> also reported the similar nature of the optical response. The details of

electron transitions are presented by drawing vertical lines (the color code represent the absorption plot of same color) as shown in Figures 7 and 8. In our calculations, (6,0) h-SWCNT is optically very active within the Vis-IR range under the reference values, and also more interestingly, the maximum absorption intensity in each value was always located within the Vis-IR range showing potential application in optoelectronic devices. For the systems with stress values of  $-5$  and  $5$  GPa, the  $\alpha_a(\omega)$  plot using the HSE06 method are also calculated for supporting the accuracy DFT-1/2 method, and the results is shown in Figure S2. In comparison with the DFT-1/2 approach, the optical responses resulting from HSE06 are of the same order as that of the DFT-1/2.

**Mechanical Properties.** The diameter dependence of the mechanical properties of CNTs [both single-walled carbon nanotubes (SWCNTs) and multi-walled carbon nanotubes (MWCNTs)] have been reported by many researchers.<sup>92–94</sup> In most of the previous work, the diameter of CNTs was modulated by the choice of different chiral indices<sup>95,96</sup> and MWCNTs with number of layers.<sup>97,98</sup> Liang et al.,<sup>99</sup> from theoretical approaches, reported the an-isotropic behavior of SWCNTs with tube diameter less than  $10$  Å. The authors also reported the difference in the elastic responses of the tube having diameter less than  $10$  Å from that of the tube with diameter greater than  $20$  Å. In this section, we are reporting the elastic behavior for (6,0) h-SWCNT under different values of compression and extension pressure. For our investigation,

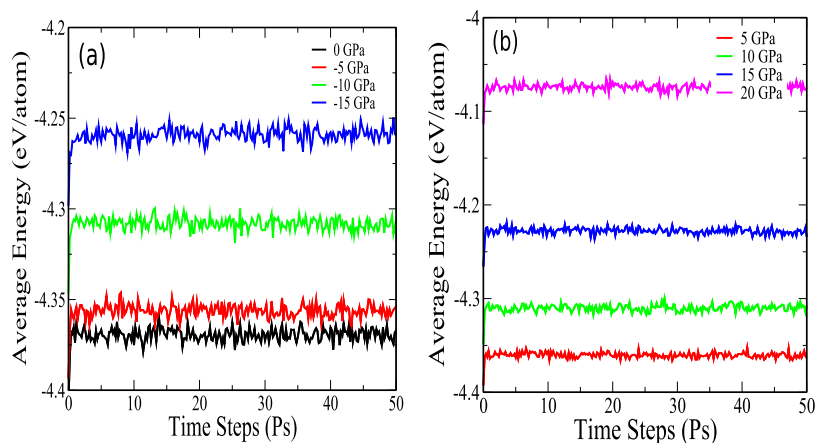


**Figure 11.** Average energy–time steps plot for (6,0)h-SWCNT under (a) compressive and (b) tensile stress.

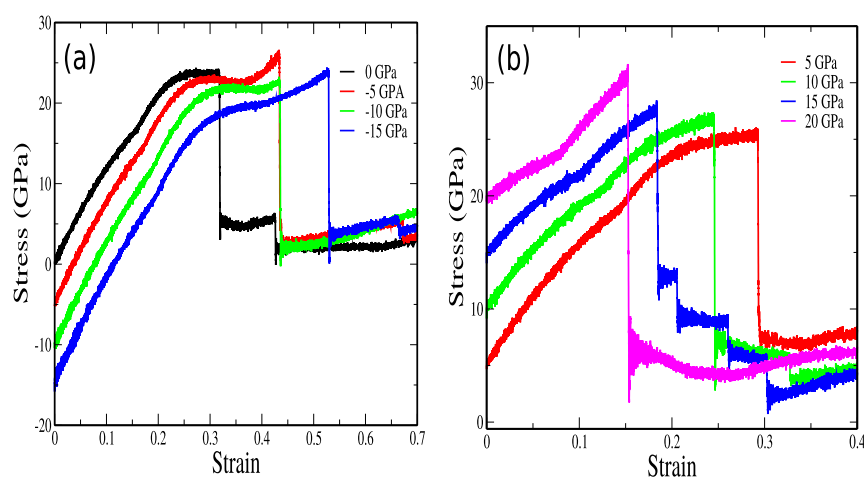


**Figure 12.** Stress–strain plot for (6,0)h-SWCNT under (a) compressive and (b) tensile stress.

we carried out a series of MD simulations using NVT Martyna Tobias Klein algorithm.<sup>100</sup>

First, the mechanical stability for all systems is investigated by calculating the average energy using MD simulations. Each system shows constant average energy over the time steps of 50 ps shown in Figure 11 which confirm that our systems are mechanically stable at room temperature.<sup>101</sup> For verification of our MD simulation results, we also check the Born–Huang criteria<sup>102</sup> for the systems with stress  $-5$  and  $5$  GPa. Six independent elastic constants ( $C_{11}$ ,  $C_{12}$ ,  $C_{13}$ ,  $C_{33}$ ,  $C_{44}$ ,  $C_{66}$ ) are required to meet Born–Huang criteria for stability ( $C_{11} > |C_{12}|$ ,  $2C_{13}^2 < C_{33}(C_{11} + C_{12})$ ,  $C_{44} > 0$ ,  $C_{66} > 0$ ). Table S4 shows that the calculated elastic constant values and the stability criteria are satisfied. For further investigation of the mechanical characteristics, the stress–strain relations are generated and shown in Figure 12.

In each stress–strain graph (see Figure 12), it is observed that the stress value increases linearly with increase in strain value at the first stage (Hooke's region). When the strain value reaches the critical failure, the corresponding stress value drops rapidly and then progressively drops to zero as the strain value is increased. A similar stress–strain trend was also reported by Yazdani et al.<sup>103</sup> The obtained failure strain for (6,0)h-SWCNT without stress (black symbol) is 0.35, which is slightly less than the pristine (6,0) SWCNT value of 0.39 (see Figure S1). But the ultimate stress was significantly reduced by

40.54% in comparison with that of pristine (6,0) SWCNT. For the systems with compressive stress, more stress results in a greater value of failure strain and also a greater linear extension (Hooke's region) in the stress–strain graph (see Figure 12a). But the ultimate stress shows no significant change with an increase in stress, and the values are in the range of  $20 \pm 5$  GPa. In the case of the systems with tensile stress, the failure strain value drops significantly with the increase of the stress and also shows the shorter linear extension region. But here, the system with higher shows greater ultimate stress value [see Figure 12(b)]. From the stress–strain graph, the Young's Modulus ( $E_y$ ) is calculated taking the slope of the linear region of the curve. In Tables 4 and 5, the obtained ultimate strength, failure strain, and  $E_y$  values of our systems are tabulated. Our

**Table 4.** Calculated Bond Length ( $\delta l$ ) in Å, Tube Diameter ( $\delta d$ ) in Å, Ultimate Stress ( $U_s$ ) in GPa, Failure Strain  $F_s$ , and Young's Modulus ( $E_y$ ) in GPa of (6,0) h-SWCNT under Compressive Stress in GPa

$P$	$\delta l$	$\delta d$	$U_s$	$F_s$	$E_y$
pristine (6,0)	1.44	4.91	40.57	0.39	1541.72
0	1.47	5.04	24.12	0.35	903.13
$-5$	1.45	5.15	27.24	0.45	599.12
$-10$	1.44	5.30	20.31	0.45	453.23
$-15$	1.43	5.38	22.12	0.55	391.74

**Table 5. Calculated Bond Length ( $\delta l$ ) in Å, Tube Diameter ( $\delta d$ ) in Å, Ultimate Stress ( $U_s$ ) in GPa, Failure Strain  $F_s$ , and Young's Modulus ( $E_y$ ) in GPa of (6,0) h-SWCNT under Tensile Stress in GPa**

$P$	$\delta l$	$\delta d$	$U_s$	$F_s$	$E_y$
5	1.49	4.95	25.23	0.30	1009.24
10	1.51	4.84	27.52	0.25	1226.75
15	1.54	4.73	28.35	0.20	1449.40
20	1.58	4.55	30.34	0.16	2072.69

calculated  $E_y$  value of 1541.721 GPa for pristine (6,0) SWCNT is very consistent with the earlier results.<sup>104</sup> After hydrogenation, the  $E_y$  value is reduced almost by 41% (903.130 GPa), which is supported by Li et al.<sup>105</sup>  $sp^2$ -hybridized C atoms in (6,0) SWCNT are converted into  $sp^3$  hybridization due to hydrogenation; i.e., the C=C is changed to C-C. As the strength of double bond is always stronger than the strength of the single bond, the  $E_y$  value reduces with hydrogenation. But in comparison with the graphyne nanotubes (GNTs), (6,0)h-SWCNT exhibits a larger  $E_y$  value than that of the GNTs.<sup>106</sup> Careful study of Table 5 shows a larger bond length and tube diameter for (6,0) h-SWCNT in comparison with that of the pristine (6,0) SWCNT as  $sp^3$ -hybridized C atoms are pulled away from their original sites deforming the stable structure of the pristine one. Under compressive stress, we have noticed a decrease in bond length whereas the tube diameter increases (Table 4). Meanwhile, under tensile stress the bond length increases and the tube diameter decreases as expected (Table 5). The  $E_y$  significantly drops with an increase in compressive stress (see Table 4). But, in case of tensile stress, the system with higher stress shows larger  $E_y$  (see Table 5). A similar trend of  $E_y$  and tube diameter ( $\delta d$ ) variations were also reported by Liang et al.<sup>99</sup> Hence, (6,0)h-SWCNT shows a wide range of variation in failure strain and  $E_y$  under external stress which is similar to the HfN<sub>2</sub> monolayer,<sup>77</sup> and also such ability offers it as a promising functionality for making flexible strain-dependent sensors.

**Conclusion.** In this work, we have studied the effect of stress on the electronic, optical, and mechanical properties of hydrogenated (6,0) SWCNT [(6,0) h-SWCNT] from first-principles DFT calculations. Under compressive stress we have observed an indirect to direct electronic band gap transition at -14 GPa. This band gaps tunability under applied stress offers the potential functionality of hydrogenated SWCNT in nanoelectronic and nanosensor devices. The effect of stress dependency on the kinematics gives reversibility in the adsorption-desorption of hydrogen atom which urged to calculate the desorption temperature ( $T_D$ ). The calculated  $T_D$  = 488.82 K at 22 GPa is very close to room temperature, an appropriate temperature for the release of hydrogen as a fuel. (6,0) h-SWCNT possesses strong optical properties along the tube axis and optically very active in the infrared region. Application of the stress resulted in strong optical absorption within the Vis-IR range as the intensity of spectra is maximum within this range, showing its applicability in optoelectronic and nanophotonic devices. The study of the mechanical properties from MD-simulations showed the reduction of the  $E_y$  for (6,0) h-SWCNT by 41% in comparison with pristine (6,0) SWCNT. The  $E_y$  have been further reduced to 391.74 GPa by applying compressive stress. However, under tensile stress,  $E_y$  has been enhanced to 2072.69 GPa. Our study

confirmed the multifunctional properties of (6,0) h-SWCNT under stress modulation.

## ■ ASSOCIATED CONTENT

### Supporting Information

The Supporting Information is available free of charge at <https://pubs.acs.org/doi/10.1021/acsomega.2c07637>.

Figure S1: Band structure for (6,0)h-SWCNT with uniaxial stress (a) -5 GPa and (b) 5 GPa using DFT-1/2 (back) and HSE06 (red). Figure S2: Absorption coefficient for (6,0)h-SWCNT with uniaxial stress -5 and 5 GPa using HSE06. Figure S3: Stress-strain plot for pristine (6,0) SWCNT. Table S1: Calculated electronic properties for (6,0)h-SWCNT under compressive stress. Table S2: Calculated electronic properties for (6,0)h-SWCNT under tensile stress. Table S3: Calculated adsorption ( $E_{ads}$ ) energies and desorption temperature ( $T_D$ ) for (6,0)h-SWCNT under compressive and tensile stress. Table S4: Calculated elastic constants  $C_{ij}$  (in GPa units) for (6,0) h-SWCNT under uniaxial stress (PDF)

## ■ AUTHOR INFORMATION

### Corresponding Authors

**Madhav Prasad Ghimire** – Central Department of Physics, Tribhuvan University, 44613 Kathmandu, Nepal;

[orcid.org/0000-0003-2783-4008](https://orcid.org/0000-0003-2783-4008);

Email: [madhav.ghimire@cdp.tu.edu.np](mailto:madhav.ghimire@cdp.tu.edu.np)

**Dibya Prakash Rai** – Physical Sciences Research Center (PSRC), Department of Physics, Pachhunga University College, Mizoram University, Aizawl 796001, India;

[orcid.org/0000-0002-3803-8923](https://orcid.org/0000-0002-3803-8923);

Email: [dibyaprakashrai@gmail.com](mailto:dibyaprakashrai@gmail.com)

### Authors

**Yumnam Thakur Singh** – Department of Physics, North-Eastern Hill University, Shillong, Meghalaya 793022, India

**Bhanu Chettri** – Department of Physics, North-Eastern Hill University, Shillong, Meghalaya 793022, India; Physical Sciences Research Center (PSRC), Department of Physics, Pachhunga University College, Mizoram University, Aizawl 796001, India

**Lalrin Kima** – Physical Sciences Research Center (PSRC), Department of Physics, Pachhunga University College, Mizoram University, Aizawl 796001, India

**Zosiamliana Renthlei** – Physical Sciences Research Center (PSRC), Department of Physics, Pachhunga University College, Mizoram University, Aizawl 796001, India

**Prasanta Kumar Patra** – Department of Physics, North-Eastern Hill University, Shillong, Meghalaya 793022, India

**Mattipally Prasad** – Department of Physics, University College of Science, Osmania University, Hyderabad 500007 Telangana, India

**Juluru Sivakumar** – Department of Physics, University College of Science, Osmania University, Hyderabad 500007 Telangana, India

**Amel Laref** – Department of Physics and Astronomy, College of Science, King Saud University, Riyadh 11451, Saudi Arabia

Complete contact information is available at:

<https://pubs.acs.org/doi/10.1021/acsomega.2c07637>

## Notes

The authors declare no competing financial interest.

## ACKNOWLEDGMENTS

A.L. acknowledges support from the “Research Center of the Female Scientific and Medical Colleges”, Deanship of Scientific Research, King Saud University, Saudi Arabia. M.P.G. acknowledges IFW-Dresden, Germany for providing the large-scale computer nodes for scientific computations. M.P.G. and D.P.R. are supported by the University Grants Commission, Nepal under UGC Grant No. CRG-78/79 S&T-03.

## REFERENCES

- (1) Kong, Q.; Shi, X.; Ma, W.; Zhang, F.; Yu, T.; Zhao, F.; Zhao, D.; Wei, C. Strategies to improve the adsorption properties of graphene-based adsorbent towards heavy metal ions and their compound pollutants: A review. *J. Hazard. Mater.* **2021**, *415*, 125690.
- (2) Rasheed, M.; Shihab, S.; Sabah, O. W. An investigation of the Structural, Electrical and Optical Properties of Graphene-Oxide Thin Films Using Different Solvents. *J. Phys. Conf. Ser.* **2021**, *1795*, 012052.
- (3) Halim, S. N. M.; Taib, M. F. M.; Ahmad, F. First Principles Study on Electronic and Optical Properties of Single Walled Carbon Nanotube for Photonics Application. *IOP Conf. Ser. Mater. Sci. Eng.* **2021**, *1051*, 012089.
- (4) Field, J. E. The mechanical and strength properties of diamond. *Rep. Prog. Phys.* **2012**, *75*, 126505.
- (5) Jo, G.; Choe, M.; Lee, S.; Park, W.; Kahng, Y. H.; Lee, T. The application of graphene as electrodes in electrical and optical devices. *Nanotechnology* **2012**, *23*, 112001.
- (6) Olabi, A. G.; Abdelkareem, M. A.; Wilberforce, T.; Sayed, E. T. Application of graphene in energy storage device â A review. *Renew. Sustain. Energy Rev.* **2021**, *135*, 110026.
- (7) Chen, H. W.; Wu, R. J.; Chan, K. H.; Sun, Y. L.; Su, P. G. The application of CNT/Nafion composite material to low humidity sensing measurement. *Sensors Actuators B Chem.* **2005**, *104*, 80–84.
- (8) Nguyen, H. S.; Luu, T. L. A.; Bui, H. T.; Nguyen, T. T.; Nguyen, H. L.; Nguyen, C. T. Facile synthesis of in situ CNT/WO<sub>3</sub>·H<sub>2</sub>O nanoplate composites for adsorption and photocatalytic applications under visible light irradiation. *Semicond. Sci. Technol.* **2021**, *36*, 095010.
- (9) Novoselov, K. S.; Jiang, D.; Schedin, F.; Booth, T. J.; Khotkevich, V. V.; Morozov, S. V.; Geim, A. K. Two-dimensional atomic crystals. *Proc. Natl. Acad. Sci. U. S. A.* **2005**, *102*, 10451–10453.
- (10) Iijima, S. Helical microtubules of graphitic carbon. *Nature* **1991**, *354*, 56–58.
- (11) Natsuki, T. Carbon Nanotube-Based Nanomechanical Sensor: Theoretical Analysis of Mechanical and Vibrational Properties. *Electron* **2017**, *6*, 56.
- (12) Georgantzinos, S. K.; Anifantis, N. K. Carbon nanotube-based resonant nanomechanical sensors: A computational investigation of their behavior. *Phys. E Low-dimensional Syst. Nanostructures* **2010**, *42*, 1795–1801.
- (13) Peng, L. M.; Zhang, Z.; Qiu, C. Carbon nanotube digital electronics. *Nat. Electron.* **2019**, *2*, 499–505.
- (14) Liu, L.; Han, J.; Xu, L.; Zhou, J.; Zhao, C.; Ding, S.; Shi, H.; Xiao, M.; Ding, L.; Ma, Z.; Jin, C.; Zhang, Z.; Peng, L. M. Aligned, high-density semiconducting carbon nanotube arrays for high-performance electronics. *Science (80-)* **2020**, *368*, 850–856.
- (15) Kim, H.; Kang, T. H.; Ahn, J.; Han, H.; Park, S.; Kim, S. J.; Park, M. C.; Paik, S. H.; Hwang, D. K.; Yi, H.; et al. Spirally Wrapped Carbon Nanotube Microelectrodes for Fiber Optoelectronic Devices beyond Geometrical Limitations toward Smart Wearable E-Textile Applications. *ACS Nano* **2020**, *14*, 17213–17223.
- (16) Ali, A. J.; Tugolukov, E. N. An experimental study on the influence of functionalized carbon nanotubes CNT Taunit series on

the thermal conductivity enhancement. *IOP Conf. Ser. Mater. Sci. Eng.* **2019**, *693*, 012001.

- (17) Il'ina, M. V.; Konshin, A. A.; Solomin, E. G. Flexoelectrical nanogenerator design using aligned carbon nanotubes. *J. Phys. Conf. Ser.* **2018**, *1124*, 071010.
- (18) Allali, F.; Chadli, H.; Rahmani, A. Theoretical study of electronic properties of nitrogen doped carbon nanotubes. *IOP Conf. Ser. Mater. Sci. Eng.* **2020**, *783*, 012015.
- (19) Tetik, E.; Karadağ, F.; Karaaslan, M.; Çömez, A. The Electronic Properties of the Graphene and Carbon Nanotubes: Ab Initio Density Functional Theory Investigation. *ISRN Nanotechnology* **2012**, *2012*, 1–7.
- (20) Ghasempour, R.; Narei, H. CNT Basics and Characteristics. *Carbon Nanotub. Polym. From Nanoscale to Macroscale* **2018**, 1–24, 1.
- (21) Rathinavel, S.; Priyadharshini, K.; Panda, D. A review on carbon nanotube: An overview of synthesis, properties, functionalization, characterization, and the application. *Mater. Sci. Eng. B Solid-State Mater. Adv. Technol.* **2021**, *268*, 115095.
- (22) Scott, C. D.; Arepalli, S.; Nikolaev, P.; Smalley, R. E. Growth mechanisms for single-wall carbon nanotubes in a laser-ablation process. *Appl. Phys. A: Mater. Sci. Process.* **2001**, *72*, 573–580.
- (23) Chrzanowska, J.; Hoffman, J.; Malolepszy, A.; Mazurkiewicz, M.; Kowalewski, T. A.; Szymanski, Z.; Stobinski, L. Synthesis of carbon nanotubes by the laser ablation method: Effect of laser wavelength. *Phys. status solidi* **2015**, *252*, 1860–1867.
- (24) Ismail, R. A.; Mohsin, M. H.; Ali, A. K.; Hassoon, K. I.; Erten-Ela, S. Preparation and characterization of carbon nanotubes by pulsed laser ablation in water for optoelectronic application. *Phys. E Low-dimensional Syst. Nanostructures* **2020**, *119*, 113997.
- (25) Zhang, D.; Ye, K.; Yao, Y.; Liang, F.; Qu, T.; Ma, W.; Yang, B.; Dai, Y.; Watanabe, T. Controllable synthesis of carbon nanomaterials by direct current arc discharge from the inner wall of the chamber. *Carbon N. Y.* **2019**, *142*, 278–284.
- (26) Chaudhary, S. K.; Singh, K. K. Complex Phenomenal Growth of Multi-walled Carbon Nanotubes in Conventional Arc Discharge Process. *Trans. Indian Inst. Met.* **2021**, *74*, 2043–2048.
- (27) Corbella, C.; Portal, S.; Zolotukhin, D. B.; Martinez, L.; Lin, L.; Kundrapu, M. N.; Keidar, M. Pulsed anodic arc discharge for the synthesis of carbon nanomaterials. *Plasma Sources Sci. Technol.* **2019**, *28*, 045016.
- (28) Manawi, Y. M.; Ihsanullah; Samara, A.; Al-Ansari, T.; Atieh, M. A. A Review of Carbon Nanomaterials' Synthesis via the Chemical Vapor Deposition (CVD) Method. *Mater.* **2018**, *11*, 822.
- (29) Esteves, L. M.; Oliveira, H. A.; Passos, F. B. Carbon nanotubes as catalyst support in chemical vapor deposition reaction: A review. *J. Ind. Eng. Chem.* **2018**, *65*, 1–12.
- (30) Singh, Y. T.; Patra, P. K.; Obodo, K. O.; Saad H.-E, M. M.; Rai, D. P. N-doped direction-dependent electronic and mechanical properties of single-walled carbon nanotube (SWCNT) from a first-principles density functional theory (DFT) and MD-simulation. *J. Mol. Graph. Model.* **2022**, *111*, 108111.
- (31) Singh, Y. T.; Patra, P. K.; Hieu, N. N.; Rai, D. P. Study of electronic and mechanical properties of single walled Carbon nanotube (SWCNT) via substitutional Boron doping in zigzag and armchair pattern. *Surfaces and Interfaces* **2022**, *29*, 101815.
- (32) Chai, G. L.; Lin, C. S.; Cheng, W. D. First-principles study of ZnO cluster-decorated carbon nanotubes. *Nanotechnology* **2011**, *22*, 445705.
- (33) Jinxiao, W.; Jianfeng, Y.; Jun, Y.; Guanjuan, Q.; Hang, W.; WangRui, H. Superior MoS<sub>2</sub>-decorated CNT composite materials for photoelectric detectors. *Opt. Mater. (Amst.)* **2018**, *86*, 113–118.
- (34) Martinez-Rubi, Y.; Ashrafi, B.; Jakubinek, M. B.; Zou, S.; Laqua, K.; Barnes, M.; Simard, B. Fabrication of High Content Carbon Nanotube-Polyurethane Sheets with Tailorable Properties. *ACS Appl. Mater. Interfaces* **2017**, *9*, 30840–30849.
- (35) Hu, T.; Qian, G.; Wu, X.; Wang, C. Mechanical behavior and micro-mechanism of carbon nanotube networks under friction. *Carbon N. Y.* **2022**, *200*, 108–115.

- (36) Kim, T.; Sridharan, I.; Zhu, B.; Orgel, J.; Wang, R. Effect of CNT on collagen fiber structure, stiffness assembly kinetics and stem cell differentiation. *Mater. Sci. Eng., C* **2015**, *49*, 281–289.
- (37) Ravanbakhsh, H.; Bao, G.; Mongeau, L. Carbon nanotubes promote cell migration in hydrogels. *Sci. Reports* **2020**, *10*, 1–10.
- (38) Pandey, R. R.; Chusuei, C. C. Carbon Nanotubes, Graphene, and Carbon Dots as Electrochemical Biosensing Composites. *Mol.* **2021**, *26*, 6674.
- (39) Shuai, C.; Peng, B.; Liu, M.; Peng, S.; Feng, P. A self-assembled montmorillonite-carbon nanotube hybrid nanoreinforcement for poly-l-lactic acid bone scaffold. *Mater. Today Adv.* **2021**, *11*, 100158.
- (40) Rahamathulla, M.; Bhosale, R. R.; Osmani, R. A.; Mahima, K. C.; Johnson, A. P.; Hani, U.; Ghazwani, M.; Begum, M. Y.; Alshehri, S.; Ghoneim, M. M.; et al. Carbon Nanotubes: Current Perspectives on Diverse Applications in Targeted Drug Delivery and Therapies. *Mater.* **2021**, *14*, 6707.
- (41) Lovell, T. C.; Bolton, S. G.; Kenison, J. P.; Shanguan, J.; Otteson, C. E.; Civitci, F.; Nan, X.; Pluth, M. D.; Jasti, R. Subcellular Targeted NanoHoop for One- And Two-Photon Live Cell Imaging. *ACS Nano* **2021**, *15*, 15285.
- (42) Mondal, J.; An, J. M.; Surwase, S. S.; Chakraborty, K.; Sutrathar, S. C.; Hwang, J.; Lee, J.; Lee, Y.-k. Carbon Nanotube and Its Derived Nanomaterials Based High Performance Biosensing Platform. *Biosensors* **2022**, *12*, 731.
- (43) Wang, Z. Chirality-dependent motion transmission between aligned carbon nanotubes. *Carbon N. Y.* **2019**, *151*, 130–135.
- (44) ThamaraiKannan, S.; Sunny, M. R.; Pradhan, S. C. Chirality dependent mechanical properties of carbon nano-structures. *Mater. Res. Express* **2019**, *6*, 095018.
- (45) Brownlie, L.; Shapter, J. Advances in carbon nanotube n-type doping: Methods, analysis and applications. *Carbon N. Y.* **2018**, *126*, 257–270.
- (46) Majles Ara, M. H.; Dehghani, Z. Improvement of the third order nonlinear optical properties of nematic liquid crystal under the influence of different compositional percentage of doped SWCNT and the external electric field. *J. Mol. Liq.* **2019**, *275*, 281–289.
- (47) Zhang, Z.; Yan, W.; Chen, Y.; Chen, S.; Jia, G.; Sheng, J.; Zhu, S.; Xu, Z.; Zhang, X.; Li, Y. Stable Doping of Single-Walled Carbon Nanotubes for Flexible Transparent Conductive Films. *ACS Nano* **2022**, *16*, 1063–1071.
- (48) Heyd, R.; Charlier, A.; McRae, E. Uniaxial-stress effects on the electronic properties of carbon nanotubes. *Phys. Rev. B - Condens. Matter Mater. Phys.* **1997**, *55*, 6820–6824.
- (49) Kumar, R.; Cronin, S. B. Optical Properties of Carbon Nanotubes Under Axial Strain. *J. Nanosci. Nanotechnol.* **2008**, *8*, 122–130.
- (50) Wagner, C.; Schuster, J.; Schleife, A. Strain and screening: Optical properties of a small-diameter carbon nanotube from first principles. *Phys. Rev. B* **2019**, *99*, 075140.
- (51) Son, J.; Lee, S.; Kim, S. J.; Park, B. C.; Lee, H. K.; Kim, S.; Kim, J. H.; Hong, B. H.; Hong, J. Hydrogenated monolayer graphene with reversible and tunable wide band gap and its field-effect transistor. *Nat. Commun.* **2016**, *7*, 1–7.
- (52) Guzmán-Verri, G. G.; Lew Yan Voon, L. C. Band structure of hydrogenated Si nanosheets and nanotubes. *J. Phys.: Condens. Matter* **2011**, *23*, 145502.
- (53) Ma, Y.; Xia, Y.; Zhao, M.; Ying, M.; Liu, X.; Liu, P. Collision of hydrogen atom with single-walled carbon nanotube: Adsorption, insertion, and healing. *J. Chem. Phys.* **2001**, *115*, 8152.
- (54) Nikitin, A.; Ogasawara, H.; Mann, D.; Denecke, R.; Zhang, Z.; Dai, H.; Cho, K.; Nilsson, A. Hydrogenation of single-walled carbon nanotubes. *Phys. Rev. Lett.* **2005**, *95*, 225507.
- (55) Zhang, G.; Qi, P.; Wang, X.; Lu, Y.; Mann, D.; Li, X.; Dai, H. Hydrogenation and hydrocarbonation and etching of single-walled carbon nanotubes. *J. Am. Chem. Soc.* **2006**, *128*, 6026–6027.
- (56) Wessely, O.; Katsnelson, M. I.; Nilsson, A.; Nikitin, A.; Ogasawara, H.; Odelius, M.; Sanyal, B.; Eriksson, O. Dynamical core-hole screening in the x-ray absorption spectra of hydrogenated carbon nanotubes and graphene. *Phys. Rev. B - Condens. Matter Mater. Phys.* **2007**, *76*, 161402.
- (57) Mercuri, F. Release of chemisorbed hydrogen from carbon nanotubes: Insights from ab-initio molecular dynamics simulations. *Int. J. Hydrogen Energy* **2017**, *42*, 21191–21197.
- (58) Denis, P. A.; Iribarne, F.; Faccio, R. Hydrogenated double wall carbon nanotubes. *J. Chem. Phys.* **2009**, *130*, 194704.
- (59) Zhu, W. D.; Wang, C. W.; Chen, J. B.; Li, D. S.; Zhou, F.; Zhang, H. L. Enhanced field emission from hydrogenated TiO<sub>2</sub> nanotube arrays. *Nanotechnology* **2012**, *23*, 455204.
- (60) Wang, R.; Sun, L.; Zhu, X.; Ge, W.; Li, H.; Li, Z.; Zhang, H.; Huang, Y.; Li, Z.; Zhang, Y.-F.; et al. Carbon Nanotube-Based Strain Sensors: Structures, Fabrication, and Applications. *Adv. Mater. Technol.* **2023**, *8*, 2200855.
- (61) Yamada, T.; Hayamizu, Y.; Yamamoto, Y.; Yomogida, Y.; Izadi-Najafabadi, A.; Futaba, D. N.; Hata, K. A stretchable carbon nanotube strain sensor for human-motion detection. *Nat. Nanotechnol.* **2011**, *6*, 296–301.
- (62) Zhou, Y.; Zhan, P.; Ren, M.; Zheng, G.; Dai, K.; Mi, L.; Liu, C.; Shen, C. Significant stretchability enhancement of a crack-based strain sensor combined with high sensitivity and superior durability for motion monitoring. *ACS Appl. Mater. Interfaces* **2019**, *11*, 7405–7414.
- (63) Choi, G.; Jang, H.; Oh, S.; Cho, H.; Yoo, H.; Kang, H. I.; Choi, Y.; Kim, S. H.; Lee, H. S. A highly sensitive and stress-direction-recognizing asterisk-shaped carbon nanotube strain sensor. *J. Mater. Chem. C* **2019**, *7*, 9504–9512.
- (64) Smidstrup, S. QuantumATK: An integrated platform of electronic and atomic-scale modelling tools. *J. Phys.: Condens. Matter* **2020**, *32*, 015901.
- (65) Ferreira, L. G.; Marques, M.; Teles, L. K. Approximation to density functional theory for the calculation of band gaps of semiconductors. *Phys. Rev. B* **2008**, *78*, 125116.
- (66) Yuan, J.-H.; Chen, Q.; Fonseca, L. R. C.; Xu, M.; Xue, K.-H.; Miao, X.-S. GGA-1/2 self-energy correction for accurate band structure calculations: the case of resistive switching oxides. *J. Phys. Commun.* **2018**, *2*, 105005.
- (67) van Setten, M. J.; Giantomassi, M.; Bousquet, E.; Verstraete, M. J.; Hamann, D. R.; Gonze, X.; Rignanese, G. M. The PSEUDODOJO: Training and grading a 85 element optimized norm-conserving pseudopotential table. *Comput. Phys. Commun.* **2018**, *226*, 39–54.
- (68) Juslin, N.; Erhart, P.; Träskelin, P.; Nord, J.; Henriksson, K. O.; Nordlund, K.; Salonen, E.; Albe, K. Analytical interatomic potential for modeling nonequilibrium processes in the WâCâH system. *J. Appl. Phys.* **2005**, *98*, 123520.
- (69) Obodo, K. O.; Noto, L. L.; Mofokeng, S. J.; Ouma, C. N.; Braun, M.; Dhlamini, M. S. Influence of Tm, Ho and Er dopants on the properties of Yb activated ZnTiO<sub>3</sub> perovskite: A density functional theory insight. *Mater. Res. Express* **2018**, *5*, 106202.
- (70) Zang, J. L.; Yuan, Q.; Wang, F. C.; Zhao, Y. P. A comparative study of Young's modulus of single-walled carbon nanotube by CPMD, MD and first principle simulations. *Comput. Mater. Sci.* **2009**, *46*, 621–625.
- (71) Zhu, R.; Pan, E.; Roy, A. K. Molecular dynamics study of the stress-strain behavior of carbon-nanotube reinforced Epon 862 composites. *Mater. Sci. Eng., A* **2007**, *447*, 51–57.
- (72) Pujari, B. S.; Gusarov, S.; Brett, M.; Kovalenko, A. Single-side-hydrogenated graphene: Density functional theory predictions. *Phys. Rev. B - Condens. Matter Mater. Phys.* **2011**, *84*, 041402.
- (73) Leamy, M. J. Calculation of phonon dispersion in carbon nanotubes using a continuum-atomistic finite element approach. *AIP Adv.* **2011**, *1*, 041702.
- (74) Garza, A. J.; Scuseria, G. E. Predicting Band Gaps with Hybrid Density Functionals. *J. Phys. Chem. Lett.* **2016**, *7*, 4165–4170.
- (75) Moses, P. G.; Miao, M.; Yan, Q.; Van De Walle, C. G. Hybrid functional investigations of band gaps and band alignments for AlN, GaN, InN, and InGaN. *J. Chem. Phys.* **2011**, *134*, 084703.
- (76) Mohanta, M. K.; De Sarkar, A. Tweaking the Physics of Interfaces between Monolayers of Buckled Cadmium Sulfide for a Superhigh Piezoelectricity, Excitonic Solar Cell Efficiency, and

- Thermoelectricity. *ACS Appl. Mater. Interfaces* **2020**, *12*, 18123–18137.
- (77) Mohanta, M. K.; Fathima, I. S.; De Sarkar, A. Exceptional mechano-electronic properties in the HfN<sub>2</sub> monolayer: a promising candidate in low-power flexible electronics, memory devices and photocatalysis. *Phys. Chem. Chem. Phys.* **2020**, *22*, 21275–21287.
- (78) Chai, G. L.; Lin, C. S.; Cheng, W. D. First-principles study of ZnO cluster-decorated carbon nanotubes. *Nanotechnology* **2011**, *22*, 445705.
- (79) Šljivančanin, Ž. Electronic properties of the partially hydrogenated armchair carbon nanotubes. *Phys. Rev. B - Condens. Matter Mater. Phys.* **2011**, *84*, 1–5.
- (80) Umeno, Y.; Sato, M.; Sato, M.; Shima, H. Buckling-induced band-gap modulation in zigzag carbon nanotubes. *Phys. Rev. B* **2019**, *100*, 4–6.
- (81) Zhang, W.; Yin, J.; Zhang, P.; Ding, Y. Strain/stress engineering on the mechanical and electronic properties of phosphorene nanosheets and nanotubes. *RSC Adv.* **2017**, *7*, 51466–51474.
- (82) Kim, H. J.; Kim, Y. J. High performance flexible piezoelectric pressure sensor based on CNTs-doped  $\alpha$ - $\beta$  ceramic-epoxy nanocomposites. *Mater. Des.* **2018**, *151*, 133–140.
- (83) Tang, Z. H.; Li, Y. Q.; Huang, P.; Wang, H.; Hu, N.; Fu, S. Y. Comprehensive evaluation of the piezoresistive behavior of carbon nanotube-based composite strain sensors. *Compos. Sci. Technol.* **2021**, *208*, 108761.
- (84) Liu, P.; Liang, J.; Xue, R.; Du, Q.; Jiang, M. Ruthenium decorated boron-doped carbon nanotube for hydrogen storage: A first-principle study. *Int. J. Hydrogen Energy* **2019**, *44*, 27853–27861.
- (85) Cardoso, G. L.; Piquini, P. C.; Khossossi, N.; Ahuja, R. Lithium-functionalized boron phosphide nanotubes (BPNTs) as an efficient hydrogen storage carrier. *Int. J. Hydrogen Energy* **2021**, *46*, 20586–20593.
- (86) Lyu, J.; Kudiarov, V.; Lider, A. An overview of the recent progress in modifications of carbon nanotubes for hydrogen adsorption. *Nanomaterials* **2020**, *10*, 255.
- (87) Joshi, H.; Shankar, A.; Limbu, N.; Ram, M.; Laref, A.; Patra, P. K.; Ismailova, O. B.; Zuala, L.; Chatterjee, S.; Rai, D. P. Pressure-Induced Enhanced Optical Absorption in Sulvanite Compound Cu<sub>3</sub>TaX<sub>4</sub> (X = S, Se, and Te): An ab Initio Study. *ACS Omega* **2022**, *7*, 19070–19079.
- (88) Joshi, H.; Thapa, R. K.; Laref, A.; Sukkabot, W.; Pachauu, L.; Vanchhawng, L.; Grima-Gallardo, P.; Musa Saad, H.-E. M.; Rai, D. P. Electronic and optical properties of cubic bulk and ultrathin surface [001] slab of CsPbBr<sub>3</sub>. *Surfaces and Interfaces* **2022**, *30*, 101829.
- (89) Ezzeldien, M.; Al-Qaisi, S.; Alrowaili, Z. A.; Alzaid, M.; Maskar, E.; Es-Smairi, A.; Vu, T. V.; Rai, D. P. Electronic and optical properties of bulk and surface of CsPbBr<sub>3</sub> inorganic halide perovskite a first principles DFT 1/2 approach. *Sci. Reports* **2021**, *11*, 1–12.
- (90) Al-Qaisi, S.; Rai, D. P.; Alshahrani, T.; Ahmed, R.; Haq, B. U.; Tahir, S. A.; Khuili, M.; Mahmood, Q. Structural, elastic, thermodynamic, electronic, optical and thermoelectric properties of MgLu<sub>2</sub> × 4 (X = S, Se) spinel compounds from ab-initio calculations. *Mater. Sci. Semicond. Process.* **2021**, *128*, 105766.
- (91) Yang, R.; Chen, Y. Y.; Guo, Y.; Shen, H.; Wang, S.; Jia, Y.; Su, W. S. A first-principles study of structural, electronic and optical properties of  $\alpha$ -Te tubular nanostructures modulated by uniaxial strain. *New J. Phys.* **2022**, *24*, 053037.
- (92) Malagù, M.; Goudarzi, M.; Lyulin, A.; Benvenuti, E.; Simone, A. Diameter-dependent elastic properties of carbon nanotube-polymer composites: Emergence of size effects from atomistic-scale simulations. *Compos. Part B Eng.* **2017**, *131*, 260–281.
- (93) Xu, T.; Qi, Z.; Tan, Y.; Tian, J.; Li, X. Effect of multiwalled carbon nanotube diameter on mechanical behavior and fracture toughness of epoxy nanocomposites. *Mater. Res. Express* **2021**, *8*, 015014.
- (94) Shen, Z.; Li, W.; Ma, J.; Zhang, X.; Zhang, X.; Zhang, X.; Dong, P.; Wang, S.; Xu, J.; Zhang, X. Theoretical predictions of size-dependent Young's and shear moduli of single-walled carbon nanotubes. *Phys. B Condens. Matter* **2021**, *613*, 412994.
- (95) Thamarai Kannan, S.; Sunny, M. R.; Pradhan, S. C. Chirality dependent mechanical properties of carbon nano-structures. *Mater. Res. Express* **2019**, *6*, 095018.
- (96) Mori, H.; Hirai, Y.; Ogata, S.; Akita, S.; Nakayama, Y. Chirality dependence of mechanical properties of single-walled carbon nanotubes under axial tensile strain. *Japanese J. Appl. Physics, Part 2 Lett.* **2005**, *44*, L1307.
- (97) Lau, K. T.; Chipara, M.; Ling, H. Y.; Hui, D. On the effective elastic moduli of carbon nanotubes for nanocomposite structures. *Compos. Part B Eng.* **2004**, *35*, 95–101.
- (98) Sakharova, N. A.; André, A. F.; Antunes, J. M.; Fernandes, J. V. Mechanical Characterization of Multiwalled Carbon Nanotubes: Numerical Simulation Study. *Mater.* **2020**, *13*, 4283.
- (99) Liang, Y.; Han, Q.; Xin, H. Elastic properties of carbon nanotubes. *J. Comput. Theor. Nanosci.* **2013**, *10*, 1061–1071.
- (100) Martyna, G. J.; Tobias, D. J.; Klein, M. L. Constant pressure molecular dynamics algorithms. *J. Chem. Phys.* **1994**, *101*, 4177.
- (101) Peng, L. M.; Zhang, Z. L.; Xue, Z. Q.; Wu, Q. D.; Gu, Z. N.; Pettifor, D. G. Stability of carbon nanotubes: how small can they be? *Phys. Rev. Lett.* **2000**, *85*, 3249–3252.
- (102) Mouhat, F.; Coudert, F. X. Necessary and sufficient elastic stability conditions in various crystal systems. *Phys. Rev. B* **2014**, *90*, 224104.
- (103) Yazdani, H.; Hatami, K.; Eftekhari, M. Mechanical properties of single-walled carbon nanotubes: a comprehensive molecular dynamics study. *Mater. Res. Express* **2017**, *4*, 055015.
- (104) Tonpheng, B.; Yu, J.; Andersson, B. M.; Andersson, O. Tensile strength and young's modulus of polyisoprene/single-wall carbon nanotube composites increased by high pressure cross-linking. *Macromolecules* **2010**, *43*, 7680–7688.
- (105) Li, X.; Xue, Q.; Liu, Z.; Ling, C.; Tao, Y.; Wu, T. Mechanical Properties of Hydrogenated Carbon Nanotubes (C<sub>4</sub>HNTs): A Theoretical Study. *J. Phys. Chem. C* **2014**, *118*, 16087–16094.
- (106) De Sousa, J. M.; Bizao, R. A.; Sousa Filho, V. P.; Aguiar, A. L.; Coluci, V. R.; Pugno, N. M.; Girao, E. C.; Souza Filho, A. G.; Galvao, D. S. Elastic properties of graphyne-based nanotubes. *Comput. Mater. Sci.* **2019**, *170*, 109153.